

See discussions, stats, and author profiles for this publication at: <https://www.researchgate.net/publication/332989768>

A Coupling Model of Distinct Lattice Spring Model and Lattice Boltzmann Method for Hydraulic Fracturing

Article in *Rock Mechanics and Rock Engineering* · May 2019

DOI: 10.1007/s00603-019-01819-3

CITATION

1

READS

302

2 authors:



Chao Jiang
UNSW Sydney

6 PUBLICATIONS 127 CITATIONS

[SEE PROFILE](#)



Gaofeng Zhao
Tianjin University

108 PUBLICATIONS 1,087 CITATIONS

[SEE PROFILE](#)

Some of the authors of this publication are also working on these related projects:



Wave propagation in discontinuous rock mass [View project](#)



Dynamic behavior and response of rock, discontinuity and underground opening [View project](#)

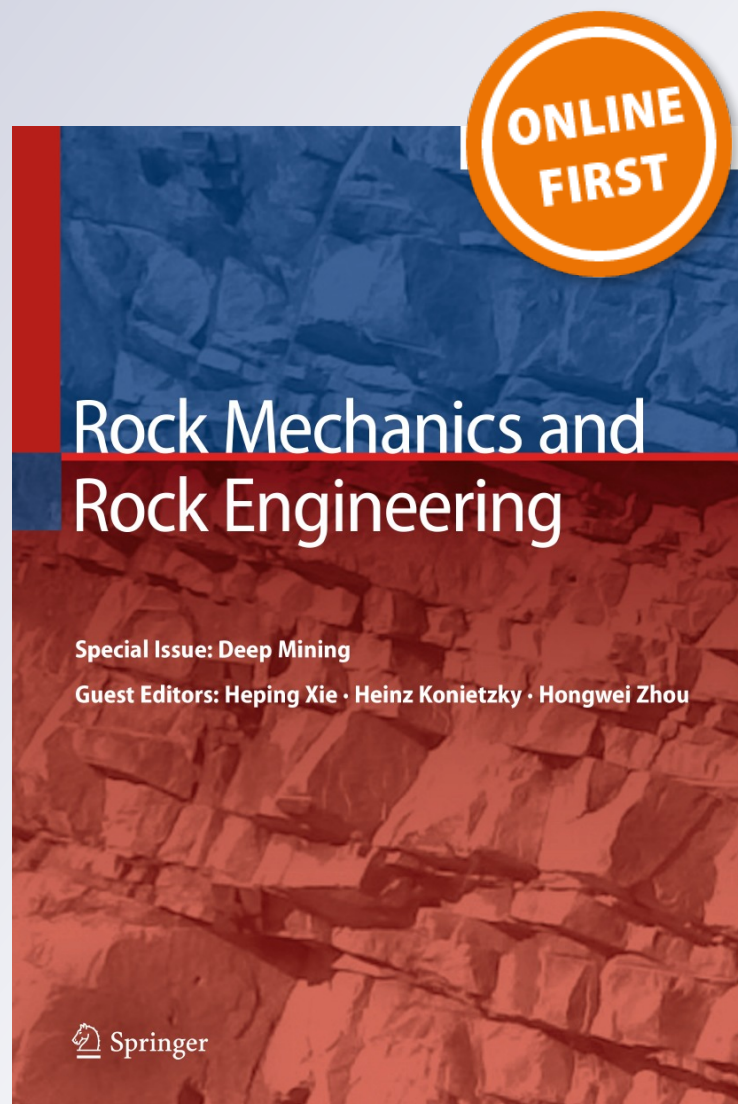
A Coupling Model of Distinct Lattice Spring Model and Lattice Boltzmann Method for Hydraulic Fracturing

Chao Jiang & Gao-Feng Zhao

Rock Mechanics and Rock Engineering

ISSN 0723-2632

Rock Mech Rock Eng
DOI 10.1007/s00603-019-01819-3



Your article is protected by copyright and all rights are held exclusively by Springer-Verlag GmbH Austria, part of Springer Nature. This e-offprint is for personal use only and shall not be self-archived in electronic repositories. If you wish to self-archive your article, please use the accepted manuscript version for posting on your own website. You may further deposit the accepted manuscript version in any repository, provided it is only made publicly available 12 months after official publication or later and provided acknowledgement is given to the original source of publication and a link is inserted to the published article on Springer's website. The link must be accompanied by the following text: "The final publication is available at link.springer.com".



A Coupling Model of Distinct Lattice Spring Model and Lattice Boltzmann Method for Hydraulic Fracturing

Chao Jiang^{1,2} · Gao-Feng Zhao¹Received: 21 December 2017 / Accepted: 21 April 2019
© Springer-Verlag GmbH Austria, part of Springer Nature 2019

Abstract

In this work, the distinct lattice spring model (DLSM) and the lattice Boltzmann method (LBM) are coupled together to simulate hydraulic fracturing problems. As the DLSM and LBM are both lattice modelling methods, the lattice meshes in these two systems are simply overlapped, which results in the same resolution in both the DLSM and LBM. The momentum exchange bounce-back algorithm is used to evaluate the forces exerted on the solid particles. Moreover, the calculation step in the LBM and DLSM is synchronised for prompt updates of fluid–solid interactions. The coupled model is further validated through a series of benchmarks. Finally, the coupled model shows its ability to simulate hydraulic fracturing in formations with complex discrete fracture networks.

Keywords Hydraulic fracturing · Distinct lattice spring model · Lattice Boltzmann method

List of symbols

Roman alphabets

a	One of the nine directions of the D2Q9 model
\tilde{a}	The opposite direction of α
α	The velocity-coupling factor from the DLSM to LBM
β	The force-coupling factor from the LBM to DLSM
b	The half-channel width
c	The basic speed on the lattice
c_s	The speed of sound in the lattice
D	The spatial dimension of the analysis
G	The pressure gradient
F	The body force term
f	The particle distribution function
f_a^{eq}	The equilibrium distribution
λ	The wall correction factor of the drag force
L_{lid}	The length of the lid-driven cavity

L_R	The length scale factor of the DLSM to a physical system
L_r	The length scale factor of the LBM to a physical system
P	The macroscopic pressure
Re	The Reynolds number
ρ	The macroscopic density
ρ_R	The density scale factor of the DLSM to a physical system
ρ_r	The density scale factor of the LBM to a physical system
ρ_{lb}	The initial density of the LBM
σ_{NS}	The far-field stresses from north or south
σ_{EW}	The far-field stresses from east or west
t_R	The time-scale factor of the DLSM to a physical system
t_r	The time-scale factor of the LBM to a physical system
k	The ratio of the diameter of the cylinder to the width of the channel
u_{max}	The maximum velocity approaching the cylinder
μ	The dynamic viscosity
U_x	The flow velocity in the X direction

Greek symbols

Δt	The time step
Δx	The lattice space width

✉ Gao-Feng Zhao
gaofeng.zhao@tju.edu.cn

¹ State Key Laboratory of Hydraulic Engineering Simulation and Safety, School of Civil Engineering, Tianjin University, Tianjin, China

² School of Civil and Environmental Engineering, The University of New South Wales, Sydney, NSW 2052, Australia

1 Introduction

To study hydraulic fracturing, numerical simulation is an effective and economic research tool in which solid–fluid interaction is the key component (Adachi et al. 2007). Conventional computational fluid dynamics (CFD) methods, such as finite element, finite volume, finite difference, discrete vortex, and B-spline methods, are commonly used to solve the Navier–Stokes equations. Nevertheless, these methods impose a substantial computational burden on automatic mesh generation and on the computation of force interactions involving solids (Hu et al. 1992) and lack important details in some special regimes. In addition, mesoscopic methods in fluid dynamics include particle-based methods such as smooth particle hydrodynamics (SPH) (Gingold and Monaghan 1977; Holmes et al. 2011), dissipative particle dynamics (DPD) (Hoogerbrugge and Koelman 1992; Liu et al. 2007), and the lattice Boltzmann method (LBM) (Yu et al. 2003; Chen and Doolen 1998). These methods can solve pore-scaled problems and are more computationally efficient than microscopic methods, such as molecular dynamics (MD). Among the mesoscopic methods, the LBM is very attractive for solid–fluid interactions by coupling with other solid simulators due to its simplicity, computational efficiency, and high scalability for parallel processing (Inamuro 2012).

The LBM has been coupled with finite-element methods (FEM) (Kwon 2008; Kwon and Jo 2008; Kollmannsberger et al. 2009; Garcia et al. 2011), discrete element methods (DEM) (Han and Cundall 2011, 2013; Leonardi et al. 2014; Zhang et al. 2014; Xue et al. 2015; Wang et al. 2016), the lattice spring model (LSM) (Buxton et al. 2005; Mora et al. 2015; Zhao 2017), etc.; the coupling with discontinuum-based methods (e.g., DEM or LSM) demonstrates the strength and flexibility of the model when applied to crack propagation and bifurcation in complex geometries. The distinct lattice spring model (DLSM) (Zhao et al. 2011) was developed to improve the computational efficiency by reducing the degrees of freedom compared to DEM without limitations on the Poisson's ratios of the conventional LSM, and its ability to simulate fracturing has been successfully demonstrated through dynamic crack propagation (Kazerani et al. 2010; Zhao et al. 2015; Jiang et al. 2017) and soil desiccation cracking (Gui and Zhao 2015). In general, the finite-discrete element method (FDEM) is closer to FEM, whereas the DLSM is closer to MD. For example, there are usually 6(12) degrees of freedom of each numerical element in 2D (3D) FDEM, whereas there are 2(3) degrees of freedom of each numerical element in 2D (3D) DLSM. Moreover, for pre-failure simulations, the FDEM has four parameters, i.e., elastic modulus, Poisson's ratio, normal stiffness of

contact (normal penalty value), and shear stiffness of contact (in cases involving shear interactions), whereas the DLSM has two parameters, i.e., normal spring stiffness and shear spring stiffness. Since the pioneering work of Munjiza et al. (1995), the FDEM has been well developed for applications such as advanced contact theory and fluid–solid coupling techniques (Ji et al. 2012; Lisjak et al. 2014). However, as a newly developed numerical model for rock mechanics, the DLSM (Zhao et al. 2011) is as yet quite undeveloped. For example, the DLSM was applied to solid–fluid interactions by introducing a fluid stream between particles under applied fluid pressure (Zhao and Khalili 2012). However, Zhao and Khalili (2012) did not consider the fluid dynamics of the setup. Fortunately, coupling the model with the LBM can simulate more realistic solid–fluid interactions, which provides the motivation for coupling the DLSM with the LBM for the first time.

The LBM is well implemented in open-source codes such as Palabos (2017) and OpenLB, which have been widely applied in many simulations (Martel and Iacono-Marziano 2015; García-Salaberri et al. 2015; Krause and Heuveline 2013). For example, Palabos illustrated a reasonable ability to predict two-phase distributions among fractured networks (Yin and Zhao 2015). However, such codes are not modifiable, and applications of the codes are limited to the functions developed in the codes. In addition, since the codes are built in certain environments (e.g., C++), it is not always feasible to integrate them with other codes. For these reasons, we developed codes called the Z-LBM and integrated them with the DLSM for hydraulic fracturing simulations. The implementation is not complicated, and the parallelisation is easy to achieve with OpenMP (Open Multi-processing). The efficiency and correctness of the code are yet to be determined. The bounce-back algorithm with an additional velocity term is adopted at the LBM and DLSM interface, and its validation is of great importance before simulating hydraulic fracturing.

The content in this paper is organised as follows. In Sect. 2, the methodology of the DLSM–LBM coupling is elaborated. The topology of the model is presented, the rules for micro and local interactions are defined, and the logic of coupling and special features is explained. In Sect. 3, the coupled model is subjected to a series of classic benchmark tests, including Poiseuille flow, lid-driven cavity flow, and flow around a stationary cylinder. In Sect. 4, various hydraulic fracture simulations are conducted by taking into consideration in situ stresses and complicated geological conditions.

2 Model Description

2.1 Brief Description of the LBM

The lattice Boltzmann method (LBM) is a meso-scale method for fluid dynamics that describes the fluid by a group of fictive particles that are located on regular lattice nodes, e.g., the D2Q9 model (see Fig. 1). In the D2Q9 model, each node has 9 lattice velocity vectors denoted as e_0 – e_8 , and it takes time Δt to propagate to nearby nodes. The fictive particle interactions are computed by collision and streaming over a discrete lattice mesh. The well-known single relaxation time is addressed by the BGK (Bhatnagar–Gross–Krook) model which describes streaming and collision with a dimensionless parameter called relaxation time (τ) defined as

$$\underbrace{f_a(\mathbf{x} + \mathbf{e}_a \Delta t, t + \Delta t)}_{\text{Streaming}} = \underbrace{f_a(\mathbf{x}, t) - \frac{[f_a(\mathbf{x}, t) - f_a^{\text{eq}}(\mathbf{x}, t)]}{\tau}}_{\text{Collision}}, \quad (1)$$

where f is the particle distribution function and f_a^{eq} is the equilibrium distribution, which is obtained by

$$f_a^{\text{eq}}(\mathbf{x}) = w_a \rho(\mathbf{x}) \left[1 + 3 \frac{\mathbf{e}_a \mathbf{u}}{c^2} + \frac{9}{2} \frac{(\mathbf{e}_a \mathbf{u})^2}{c^2} - \frac{3}{2} \frac{\mathbf{u}^2}{c^2} \right], \quad (2)$$

where w is 0 for particles at rest, 1/9 for the directions on the major axis, and 1/36 for diagonal weights, c is the basic speed on the lattice, and \mathbf{u} is the velocity vector. The relationship between the relaxation time (τ) and kinematic viscosity ν in the D2Q9 model is

$$\tau = \frac{\nu}{c_s^2 \Delta t} + \frac{1}{2}, \quad (3)$$

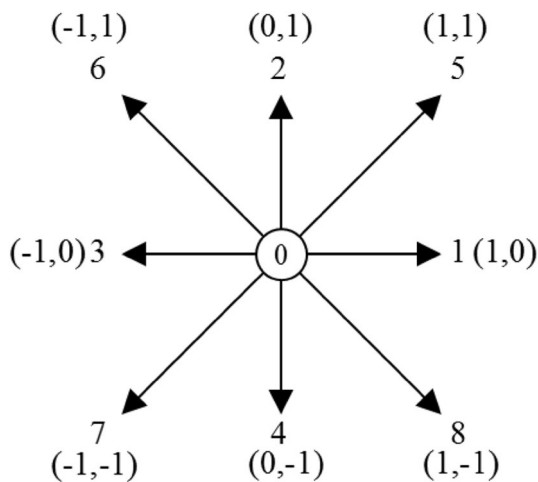


Fig. 1 D2Q9 model

where c_s is the speed of sound in the lattice. For simplicity of implementation, the value of the lattice space and time step is preferentially set as 1, i.e., $\Delta x = \Delta t = 1$, so that the lattice speed $c = 1 \text{ luts}^{-1}$ and the speed of sound $c_s = 1/\sqrt{3} \text{ luts}^{-1}$. Therefore, the dynamic viscosity becomes

$$\nu = \frac{1}{3} \left(\tau - \frac{1}{2} \right), \quad (4)$$

where τ is the relaxation time, usually with the value of (0.5, 1].

The two macroscopic parameters (i.e., density ρ and velocity \mathbf{u}) are calculated as

$$\rho = \sum_{a=0}^8 f_a \quad (5)$$

$$\mathbf{u} = \frac{1}{\rho} \sum_{a=0}^8 f_a \mathbf{e}_a \quad (6)$$

and the equation of state relating pressure P and density is

$$P = c_s^2 \rho = \frac{\rho}{3}. \quad (7)$$

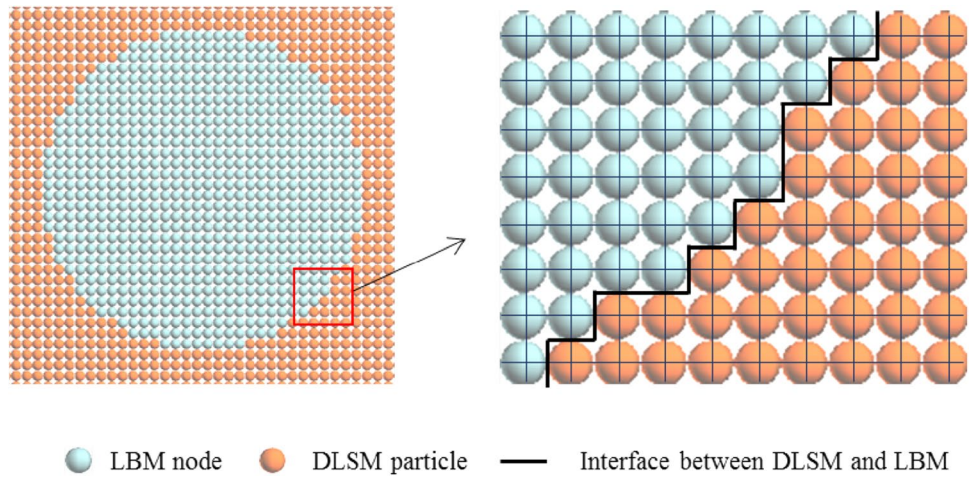
The algorithms are implemented into an LBM solver called the *Z-LBM* using C++ with OpenMP.

2.2 Topology of the Coupled Model

Another lattice modelling method, the DLSSM, also allocates its particles at the lattice nodes. Therefore, the lattice mesh in the DLSSM and LBM can be easily overlapped. Figure 2 shows an example of the topology for a square solid, surrounding cylindrical fluid in the centre. Every lattice node is filled with either a DLSSM particle or LBM node. For comparison, in DEM–LBM coupling (e.g., Xue et al. 2015), the DEM particle is much larger than the LBM grid size, so the resolution of the DEM is less than that of LBM, which reduces the computational cost for the solid solver. However, this approach increases the complexity in the implementation of solid force summation, because the DEM particle may cover different bundles of LBM unwetted nodes during the simulation. In addition, the decrease in solid resolution is not beneficial to the accuracy of the solid simulation.

It is also noted that the interface between the DLSSM and LBM is stairwise. The stairwise feature does cause inaccuracy in the presentation of the curved boundary, but does not have much influence on the results with adequate resolution, which will be discussed in Sect. 3. Several assumptions were made in our coupled model. For the LBM, no fluid lag is permitted at crack propagation tips, and the medium is fully saturated with no leaks. For the DLSSM, only small

Fig. 2 Representation of the topology of the coupled model. DLSPM and LBM share the same lattice network in the calculation domain and form stairwise interface



deformations are allowed, i.e., the deformation of the solid skeleton is small and does not cause a significant volumetric change in the fluid.

2.3 Local Rules for Fluid Nodes

Normal collision and streaming processes are conducted when the neighbouring node of a fluid node is another fluid node. A simple bounce-back algorithm with an additional momentum term is applied when the neighbouring node is a velocity-conditioned fluid node or solid particle.

2.3.1 Fluid Node to Fluid Node Subject to Velocity Boundary Conditions

While there are several methods to implement boundary conditions in the LBM, a simple but effective velocity boundary condition is primarily applied in the *Z-LBM*. We refer to the fluid node x_v at which the velocity boundary condition is applied, and the streaming particle distribution is calculated based on the incoming particle distribution by considering the additional momentum term due to the velocity u_v , which is

$$\tilde{f}_a(x_v, t + \Delta t) = f_a(x_v, t) - 2\rho_v w_a (e_a \cdot u_v) / c_s^2, \quad (8)$$

where $\tilde{f}_a(x_v, t + \Delta t)$ is the streaming particle distribution function in the opposite direction of $f_a(x_v, t)$, ρ_v is the fluid density at node x_v , w_a is the weighting factor in the direction a (one of the nine directions in Fig. 1), u_v is the applied value for the velocity boundary condition, and c_s is the speed of sound in LBM.

2.3.2 Fluid Node to Solid Particle

The same algorithm as in the velocity boundary condition [i.e., Eq. (8)] is applied for the solid particle. If the particle is at rest, simple bounce-back is applied (with $u_v = 0$). If

the particle is moving, the velocity of that particle is considered in the additional momentum term. Therefore, the boundary-conditioned nodes and the solid nodes are treated as “bounce-back” nodes. It is assumed that we are dealing with nearly incompressible flow, so ρ_v at the boundary node can be easily set to ρ_f in the neighbouring fluid nodes.

2.3.3 Body Force

The body force, which can represent the gravitational force or the force due to applied pressure, can be incorporated by adding another term to the streaming particle distribution function, such that Eq. (1) becomes (Mohamad and Kuzmin 2010)

$$f_a(x + e_a \Delta t, t + \Delta t) = f_a(x, t) - \frac{[f_a(x, t) - f_a^{eq}(x, t)]}{\tau} + \frac{w_a(e_a F) \Delta t}{c_s^2} \quad (9)$$

and Eq. (8) becomes

$$\tilde{f}_a(x_v, t + \Delta t) = f_a(x_v, t) - 2\rho_v w_a (e_a \cdot u_v) / c_s^2 + \frac{w_a(e_a F) \Delta t}{c_s^2}, \quad (10)$$

where F is the body force term.

2.4 Force Exerted on Solid Particles

The force on the solid particle is evaluated with a momentum exchange algorithm between the fluid and solid nodes. Therefore, the first step is to detect the boundary nodes at which the force is evaluated. This is done by executing search loops for every single solid particle. As an example, in Fig. 3, the search for the central particle includes eight directions, as the arrows indicate. When at least one fluid node is detected, the particle is marked as a boundary node.

Figure 4 plots the particle distribution function in and out of the solid boundary node. In the bounce-back algorithm,

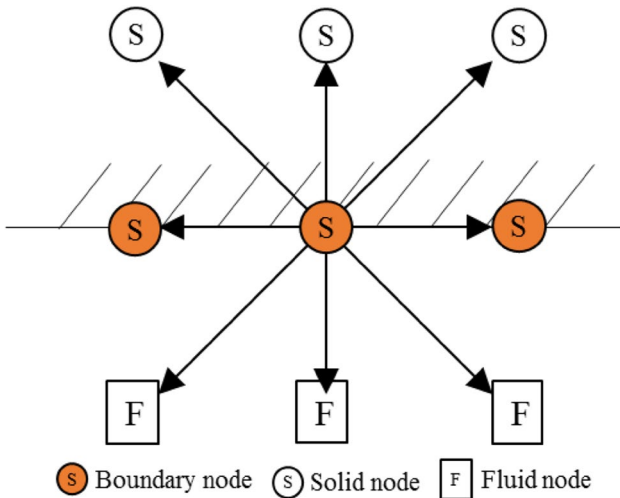


Fig. 3 Algorithm for detection of boundary nodes

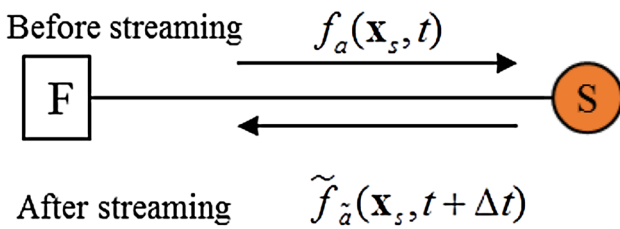


Fig. 4 Particle distribution functions before and after streaming at the boundary node

the particle distributions that are received are reflected back. In addition, the velocity of the solid node is considered with an additional momentum term. Therefore, in the momentum

exchange algorithm, the force evaluated at the boundary nodes in the direction a is calculated as

$$\begin{aligned}
 F_a\left(t + \frac{\Delta t}{2}\right) &= \left[\mathbf{e}_a f_a(\mathbf{x}_s, t) - \mathbf{e}_a \tilde{f}_a(\mathbf{x}_s, t + \Delta t) \right] \frac{\Delta x^D}{\Delta t} \\
 &= \left[\mathbf{e}_a f_a(\mathbf{x}_s, t) - \mathbf{e}_a \left[f_a(\mathbf{x}_s, t) - 2\rho_s w_a (\mathbf{e}_a \cdot \mathbf{u}_s) / c_s^2 \right] \right] \frac{\Delta x^D}{\Delta t} \quad (11) \\
 &= \mathbf{e}_a \left[2f_a(\mathbf{x}_s, t) - 2\rho_s w_a (\mathbf{e}_a \cdot \mathbf{u}_s) / c_s^2 \right] \frac{\Delta x^D}{\Delta t},
 \end{aligned}$$

where Δx and Δt are lattice space and time step in the LBM, which are set as one for simplicity; D is the spatial dimension of the analysis (set as two in this work); and ρ_s is the density at the neighbouring fluid node. The total force at a solid particle is the sum of all components from neighbouring fluid nodes.

2.5 Crack Propagation Logic

The springs in the DLSSM deform according to the magnitudes of fluid forces and contact forces, and the crack propagation is caused by the natural breakages of the springs. An example of a setup is shown in Fig. 5 for a clear understanding of the propagation of a crack. In Fig. 5, the fluid nodes are subject to a velocity boundary condition on the left. One spring at Step n breaks, which causes the two red DLSSM particles to be detected as broken particles. In addition, all the springs attached to the broken particles are removed. In the next time step, the LBM nodes substitute the broken solid particle and are included in the new LBM calculation cycle. In this way, the crack propagates with the increase in Δx , and all the neighbouring particles surrounding the new

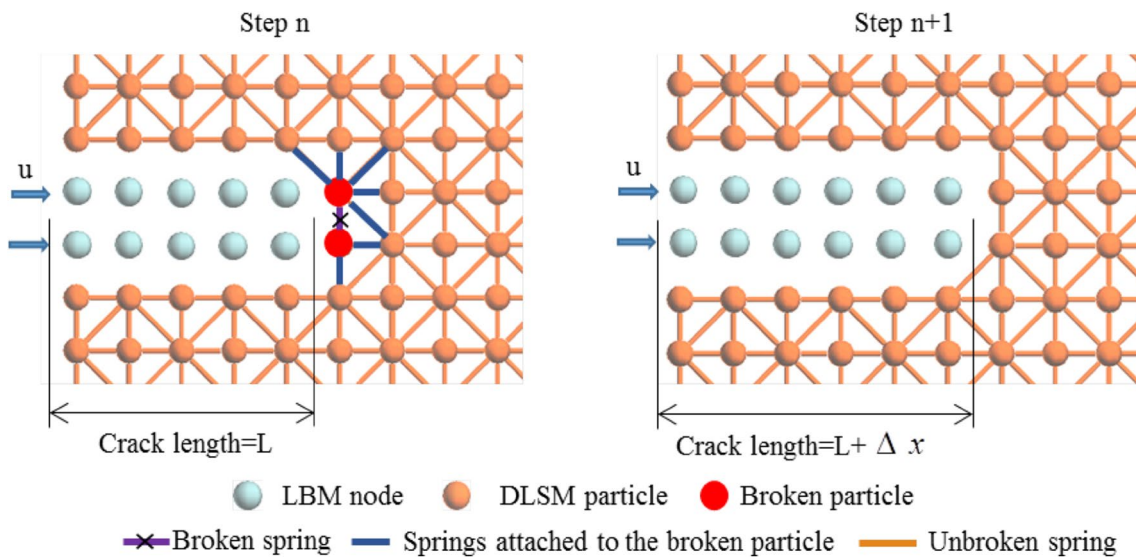


Fig. 5 Schematic diagram for the crack propagation

fluid nodes become boundary nodes. It is noted that more than one solid spring could break in a calculation step.

2.6 Direct Coupling of the DLSM and LBM

The system consists of two solvers, one solid solver, the DLSM, and one fluid solver, the *Z-LBM*. The coupling scheme is shown in Fig. 6. The left cycle is the DLSM calculation cycle, and the right cycle is the LBM cycle. The two cycles work independently, but also influence each other. The DLSM updates the fluid domain and modifies the collision term in the LBM, and the LBM adds an additional force term to the equation of motion in the DLSM (Zhao et al. 2011; Jiang and Zhao 2017). In a macroscopic view, the DLSM influences the velocity and pressure of the fluid, while the LBM imposes hydrodynamic forces on the solid. Specifically, the influences from the DLSM solver are observed in two of the steps. After the relative particle displacement is calculated, the new “bounce-back” nodes are defined when the particles are broken, which also influences

the procedure of bounce-back in the LBM loop. The other step is to calculate the momentum term for moving solid nodes with the particle velocities from the DLSM converted before use. The conversion will be introduced in Sect. 2.7. The influence on the DLSM loop is only one step in the implementation. The force on the DLSM particle is updated with the fluid force from the LBM loop in addition to internal contact forces.

Apart from the distinct feature in DLSM–LBM coupling, that two solvers share the same lattice mesh, another feature is that the calculation steps in the two solvers are synchronised. In FEM–LBM coupling, one step of the solid solver requires N steps of the LBM solver (Kollmannsberger et al. 2009), while in DEM–LBM coupling, one step in the fluid solver requires N steps of the solid solver. In fact, for either case, the interaction cannot be promptly updated and can lead to unrealistic results. Although the synchronisation of the calculation steps in DLSM–LBM coupling will increase the computational cost, it can ensure the accuracy trace of the crack tip in every calculation loop.

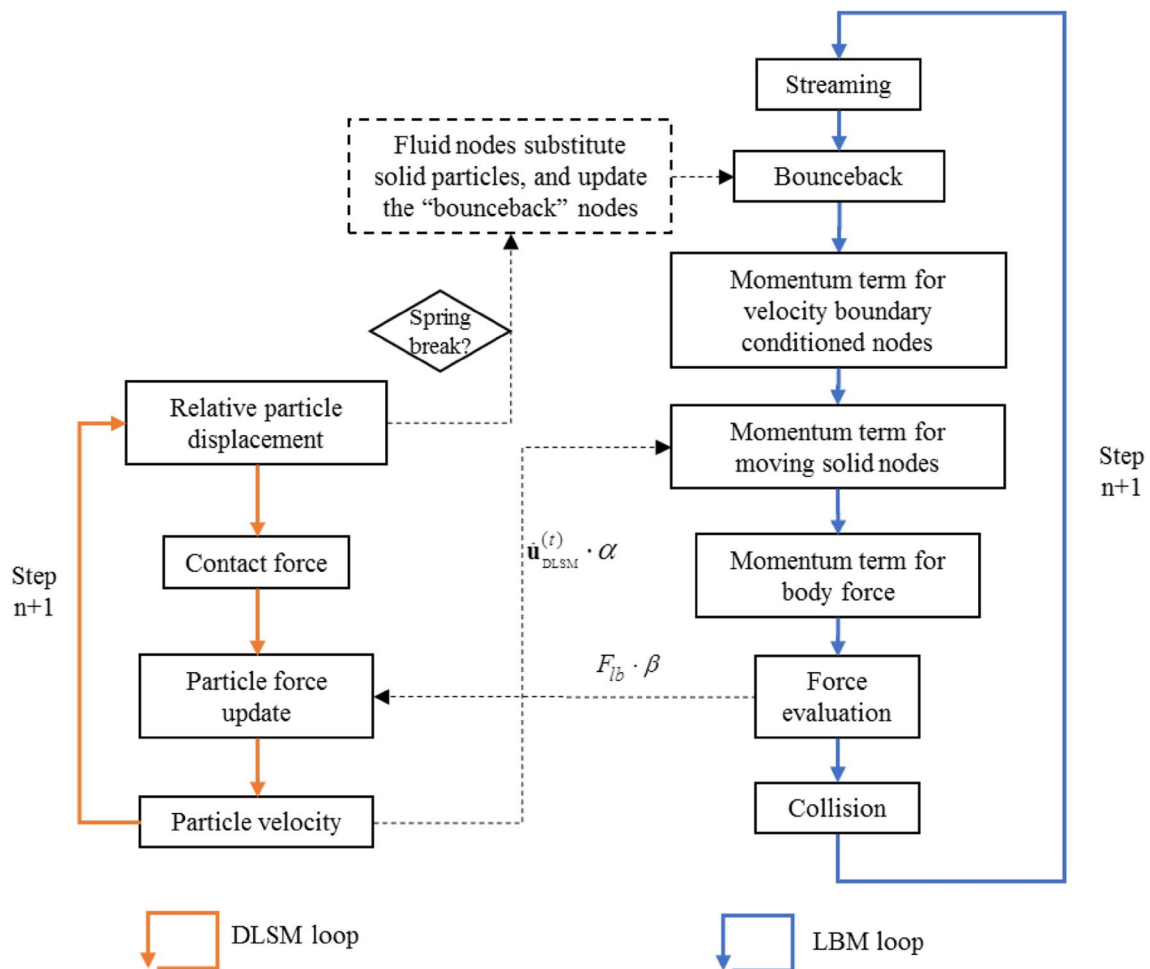


Fig. 6 Calculation cycles in coupled DLSM/LBM

Table 1 Relationship between the LBM and physical system

Name	LBM	Physical system	Conversion factor
Length	$L_{lb} = N \times \Delta x$	L_p	$L_r = \frac{L_p}{L_{lb}}$
Viscosity	$\nu_{lb} = \frac{1}{3} \left(\tau - \frac{1}{2} \right) \frac{\Delta x^2}{\Delta t}$	ν_p	$\nu_r = \frac{L_r^2}{t_r}$
Density	$\rho_{lb} = 1$	ρ_p	$\rho_r = \frac{\rho_p}{\rho_{lb}}$
Velocity	u_{lb}	u_p	$u_r = \frac{L_r}{t_r}$
Force	F_{lb}	F_p	$F_r = \rho_r \frac{L_r^3}{t_r^2}$
Pressure	P_{lb}	P_p	$P_r = \rho_r \frac{L_r^2}{t_r^2}$

2.7 Unit Conversion in the Coupled System

In the LBM, it is preferred to set the value of the discretised space Δx and discretised time Δt to one, along with the initial density ρ_{lb} . To obtain meaningful results for a physical system, conversion is needed. The conversion factors are defined with a subscript symbol r in Table 1. To start the conversion, some primary conversion factors (e.g., length L , time t , and density ρ) need to be determined first, and then, secondary conversion factors can be uniquely derived. It is noted that the time factor t_r can be obtained through the relationship $\nu_r = \frac{L_r^2}{t_r}$.

Similarly, there are conversions from the DLSTM to the physical system, with the factors followed by a subscript R . It is noted in Fig. 6 that there are interactions between the DLSTM and LBM that affect the velocity and force, so that the value should be properly scaled, i.e., $u_{lb} = u_{DLSTM} \times \alpha$ and $F_{DLSTM} = F_{lb} \times \beta$. The interface of DLSTM and LBM unit conversion is the physical system; thus, their relationships are expressed as

$$\alpha = \frac{L_R t_r}{L_r t_R} \tag{12}$$

and

$$\beta = \frac{\rho_r L_r^3 t_r^2}{\rho_R L_R^3 t_R^2} \tag{13}$$

As in our coupling scheme, the resolution of the DLSTM is the same as the LBM, i.e., one particle position corresponds to one fluid grid point, and the values of L_R and L_r are equal. Therefore, Eq. (12) and Eq. (13) become $\alpha = \frac{t_r}{t_R}$ and $\beta = \frac{\rho_r t_R^2}{\rho_R t_r^2}$, respectively.

3 Validations of the Model

The validations are first conducted on the classic Poiseuille flow model and lid-driven cavity flow for the verification of the Z-LBM. The solid–fluid interaction is validated through the model with the flow around a cylinder. For computing fluid dynamics (CFD), especially the LBM, dimensionless parameters were widely used. For example, in the following simulations, the value of the lattice length was one, the time step was one, the speed of sound was 1/3, and the relaxation time τ was one. The analytic and numerical solutions from the previous literature were also presented in a dimensionless manner. Therefore, a direct comparison can be performed.

3.1 Poiseuille Flow

Poiseuille flow is a classic problem in which laminar flow is driven by a linear pressure gradient between two parallel plates. The well-known analytical solutions yield

$$U_x(y) = \frac{G}{2\mu}(b^2 - y^2) \tag{14}$$

and

$$U_{average} = \frac{G}{3\mu}b^2, \tag{15}$$

where U_x is the flow velocity in the X direction, G is the pressure gradient ($P_{in} - P_{out}$)/ L or a gravitational pressure gradient, μ is the dynamic viscosity, b is the half-channel width (refer to Fig. 7), and y is the position in the Y -axis. Twenty nodes in each of the X and Y directions are used for the LBM simulation, and they are driven by the body force of $1e^{-9} \mu.u.l.u.ts^{-2}$. The results shown in Fig. 7 indicate

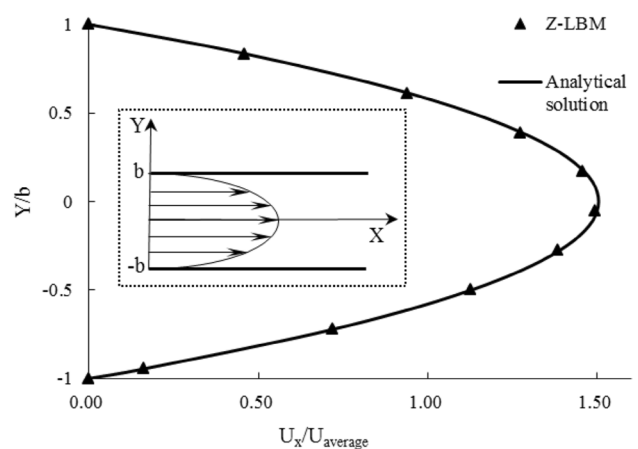


Fig. 7 Velocity distribution at the inlet in pressure-driven Poiseuille flow

excellent agreement for the horizontal fluid velocities between the simulation and the analytical solutions, and the peak velocity is 3/2 of the average velocity.

The efficiency of the *Z-LBM* is demonstrated by comparison with the well-developed open-sourced simulator *Palabos* (Palabos 1.5r), and the comparison is performed on the Poiseuille flow with different resolutions. The time spent for 20,000 loops in the LBM algorithm by single core is recorded and plotted in Fig. 8, from which we conclude that the efficiency of the *Z-LBM* is acceptable, because it only doubles the time from *Palabos* at the resolution of one million grids.

3.2 Lid-Driven Cavity Flow

The second validation of the model is on the classic lid-driven cavity flow. The model is 400 by 400 lattice nodes, and the top lid is driven by a constant velocity towards the right. The Reynolds number ($Re = \frac{U_x L_{lid}}{\nu}$) is set to 100, 400, and 1000 in three cases for comparison with the trustworthy finite-difference method by Ghia et al. (1982). The velocity contours of the case with $Re = 100$ in the *X* and *Y* directions are illustrated

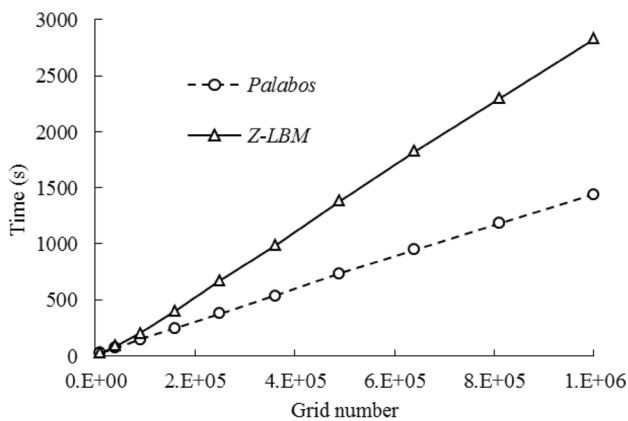
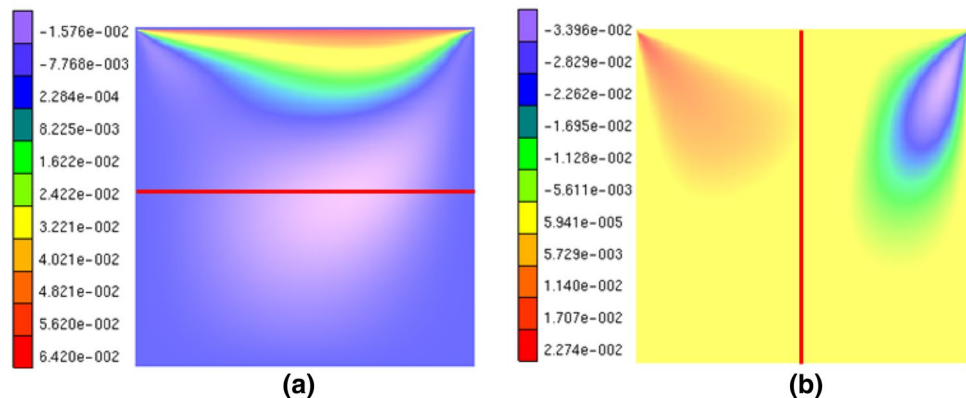


Fig. 8 Comparison of the computational efficiency between Z-LBM and Palabos. The time is denoted for 20,000 LBM loops

Fig. 9 Velocity contour plot with $Re = 100$ in **a** *X* direction **b** *Y* direction



in Fig. 9, and the horizontal and vertical lines indicated refer to the locations, where the corresponding velocities are extracted for all three cases, in Figs. 10 and 11, respectively. The LBM results agree well with the finite-difference method for different Reynolds numbers.

3.3 Flow Around an Obstacle

In the following examples, a circular cylinder is subject to the Poiseuille flow, as shown in Fig. 12. The cylinder is placed in the middle of the channel, so that only the drag force is exerted on the cylinder rather than the lift force. A constant flow velocity is applied on the left boundary of the domain, which develops to a parabolic velocity profile near the inlet. The upper and lower boundaries are treated as non-slip conditions for the bounce-back algorithm.

3.3.1 Wall Correction Factors at a Very Low Reynolds Number

The first example is with the very low Reynolds number of $2e^{-4}$, as in Richou et al. (2004) for comparison. The wall correction factor of the drag force is

$$\lambda(k) = \frac{F(k)}{\nu u_{\max}}, \tag{16}$$

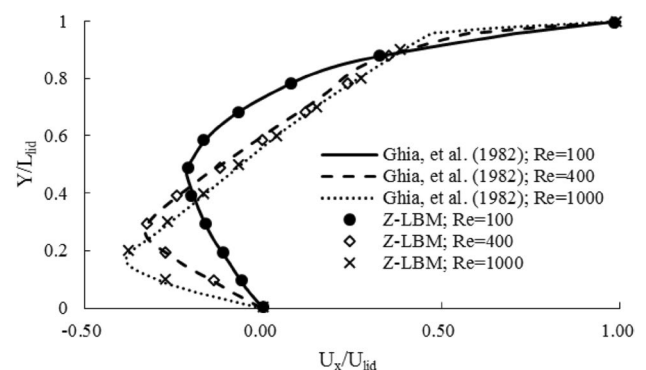


Fig. 10 Profile of *X* velocity on a vertical line in the middle

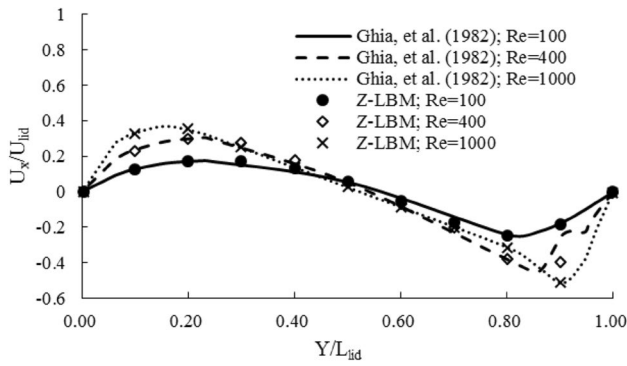


Fig. 11 Profile of Y velocity on a horizontal line in the middle

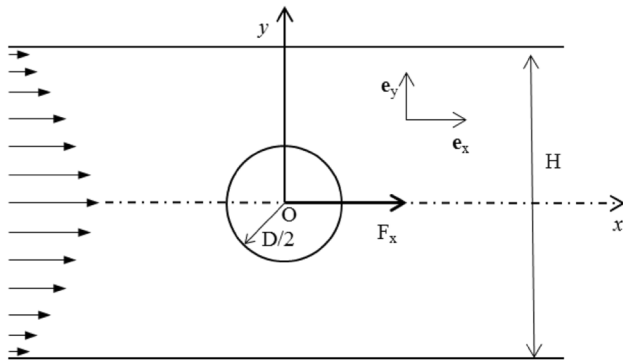


Fig. 12 Geometry of a flow passing a circular cylinder

Table 2 Comparison on the value of λ to FDM (Richou et al. 2004) and analytical results (Faxén 1946)

k	DLSM-LBM	FDM	Error%	Analytical result	Error%
0.1	8.9641	9.1630	2.23	8.9060	0.65
0.2	16.3071	16.3585	0.32	16.2072	0.62
0.3	28.1400	28.4828	1.23	27.8979	0.87
0.4	49.1080	48.8511	0.53	48.6229	1.00
0.5	89.8452	88.8184	1.11	92.3235	2.68

where k is the ratio of the diameter of the cylinder to the width of the channel (D/H), ν is the kinematic viscosity, and u_{\max} is the maximum velocity approaching the cylinder. In our simulation, the dimension of the channel is $1000 \text{ lu} \times 400 \text{ lu}$, and the diameter of the cylinder is set according to k , which varies from 0.1–0.5, with a minimum diameter of 40 lu. The results for λ are shown in Table 2. Compared to the results from the finite-difference method (Richou et al. 2004) or analytical method (Faxén 1946), the accuracy of the stairwise momentum exchange bounce-back in the coupled model is satisfactory.

Table 3 Calculated drag coefficient with comparison to immersed boundary method from Han and Cundall (2011)

Re	1	10	20	30	40
DLSM-LBM	16.8423	3.4591	2.4133	2.0050	1.7766
IBM	16.6074	3.4032	2.3634	1.9467	1.7238
Difference%	1.41	1.64	2.11	3.00	3.07

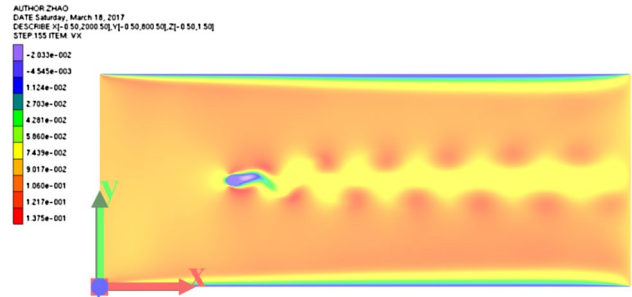


Fig. 13 Effect of Karmen vortex street for $Re = 100$; $C_d = 1.26$

3.3.2 Drag Coefficient

The calculation domain is $400 \text{ lu} \times 400 \text{ lu}$, and the diameter of the cylinder is 20 lu. The flow velocity at the inlet is set to 0.1 lu/ts. The target Reynolds number is achieved by changing the dynamic viscosity. The results for Re from 1–40 are listed in Table 3. Compared to the immersed boundary method from Han and Cundall (2011), the stairwise momentum exchange bounce-back gives satisfactory results even with a small diameter of 20 lu. For the case of $Re = 100$, the length of the channel should be long enough for the development of the Karman vortex street. The calculation domain is $2000 \text{ lu} \times 800 \text{ lu}$. The cylinder with a diameter of 50 lu is placed at a distance of 500 lu from the inlet. Unlike the results for low Reynolds number cases, where the drag force remains constant in steady state, the drag force oscillates between an upper and lower limit due to the effect of the Karman vortex street (refer to Fig. 13). The average drag coefficient is 1.2622 for $Re = 100$, which is close to the finite volume solution of 1.28 from Braza et al. (1986).

4 Simulations of Hydraulic Fracturing

In the following simulations, the LBM parameters were the same as in the previous examples. The additional mechanical parameters for the DLSM were a density of 1400 kg/m^3 , a Young's modulus of 0.41 GPa, a Poisson's ratio of 0.19, and a tensile strength of 2.4 MPa. These parameters can be directly inputted into the DLSM. The ultimate deformation of the normal spring is estimated as $\sigma_c d / E = 5.85 \times 10^{-3} \text{ lu}$.

4.1 Non-planar Hydraulic Fracture Propagation

There are many reports on non-planar hydraulic fractures under the influence of deviated stresses by different methods, such as XFEM (Wang 2015) and FEM (Men et al. 2013), in which the crack propagation is in the direction of the maximum principle stress. To illustrate the ability of the proposed coupled model on non-planar hydraulic crack propagation, a near-wellbore region with an initial perforation is simulated (refer to Fig. 14a). The dimension of the calculation domain is 300 mm \times 300 mm, and the diameter of the wellbore is 50 mm. The perforation length is 19 mm at 60° to the east–west direction. The model is pre-loaded with two principle stresses representing the far-field stresses in the direction from north or south (σ_{NS}) and those from east or west (σ_{EW}). The injection of fluid is simulated by imposing constant velocity boundary conditions outside a box that lies inside the borehole (refer to Fig. 14a). In this manner, additional values of particle distribution functions are added to the system to increase the pressure. In Fig. 14b–g, σ_{EW} is held constant, and the value for σ_{NS} is set to achieve different ratios of σ_{NS}/σ_{EW} . As shown in Fig. 14b–f, the cracks initiate at the perforation tips and then propagate in the direction of least resistance, which is perpendicular to the minimum horizontal stress. The crack path changes direction, as the ratio of the deviated stress changes. In Fig. 14d, the crack does not tilt due to the balanced horizontal stresses. In Fig. 14g, while σ_{EW} is much less than σ_{NS} , the cracks even initiate from the sides of the wellbore rather than the perforation tips. We consider that the mechanism of the crack path change shown in Fig. 14 could be the variation of the loading condition from Mode-I dominated to mixed-mode dominated for the different ratios of. Similar phenomena were also experimentally observed for PMMA plates under bi-axial loading (Hawong et al. 1987). All these simulations have successfully demonstrated the capability of the coupled model for non-planar hydraulic fracturing.

4.2 Simulation of the Hydraulic Fracturing Experiment

An injection experiment from a borehole with an unconfined block was designed to examine the predictability of the coupled model. The setup of the experiment is shown in Fig. 15a. Water is directly pumped into the hole of the specimen by flexible conduits, and the controlling valve, which is initially open, is closed slowly to increase the water pressure on the specimen at a low rate, while the pressure is recorded by a pressure sensor connected to an oscilloscope. During the experiment, vertical stress is applied through a flat plate being pressed downwards to prevent splitting the block in the weak Z direction. The applied stress does not affect the crack path, and the impact on the fracture pressure is minimal.

Brittle, gypsum-like 3D printed material is chosen as the material for hydraulic fracturing due to its ease of preparation, high homogeneity, and flexibility in geometric design (Jiang et al. 2016). The printed specimens are post-processed with cement, as a curing agent, to improve impermeability. The blocks subject to fracturing are 30 mm in edge (refer to Fig. 15b). A perforated borehole for injection, 5 mm in diameter, is located at the centre of the top surface with a depth of 27.2 mm and left 2.8 mm thickness for sealing (see side view in Fig. 15c). In addition, a pair of preset cracks with a width of 2 mm are placed adjacent to the borehole, each with a distance of 2.8 mm from the top and bottom. There are four types of designed blocks with differences in the internal cracks, as shown in Fig. 15b. In type I, the preset crack is horizontal. In type II, the crack is rotated 45°. In type III, there is one additional inclined crack with a ° inclination. In type IV, there are two inclined cracks. After printing, powdered material remains in the borehole, and the attached cracks can be extracted from the borehole. However, the inclined cracks that are unattached to the hole are designed to be straight through the specimen vertically, so that the powder can be blown away easily by a wind wand. To minimise the disturbance on the specimen when inserting a water injector into the hole, a screw joint is designed that sits above the neck of the specimen. Therefore, during the test, the screw from the water tube can be directly connected to the specimen to avoid any problems with the seal. In 3D-printed specimens, the precracks attached to the hole are internally designed, and the hole is connected to the pump by a water tube to eliminate sealing problems. For the unattached cracks that are straight through, some 3D-printing powder fully saturated with the cement-curing agent is applied to seal the openings at the top and bottom surfaces. To prevent breakage of the neck during screwing, a strong adhesive is applied at the neck and the screw joint to provide adequate strength.

The resolution in the coupled model is 300 μm \times 300 μm . The fluid domain covers the whole area of the specimen, so that the full development of the crack is captured. The cracks are completely filled with fluid. The injection of fluid is simulated by imposing a constant velocity boundary condition outside a box that is placed inside the borehole. In this manner, additional values on particle distribution functions are added to the system to increase the pressure. The predicted fracture paths are shown in Fig. 16a, which agrees well with the paths in hydraulic fracturing tests on homogeneous 3D-printed specimens. The fluid pressure at the peak, where the crack reaches the edge is recorded. The pressure is scaled and the parameters of the model are calibrated with the average peak pressure in the type I model in the experiment. As shown in Fig. 16b, the trend of the peak pressure in the coupled model is similar to the overall trend of the

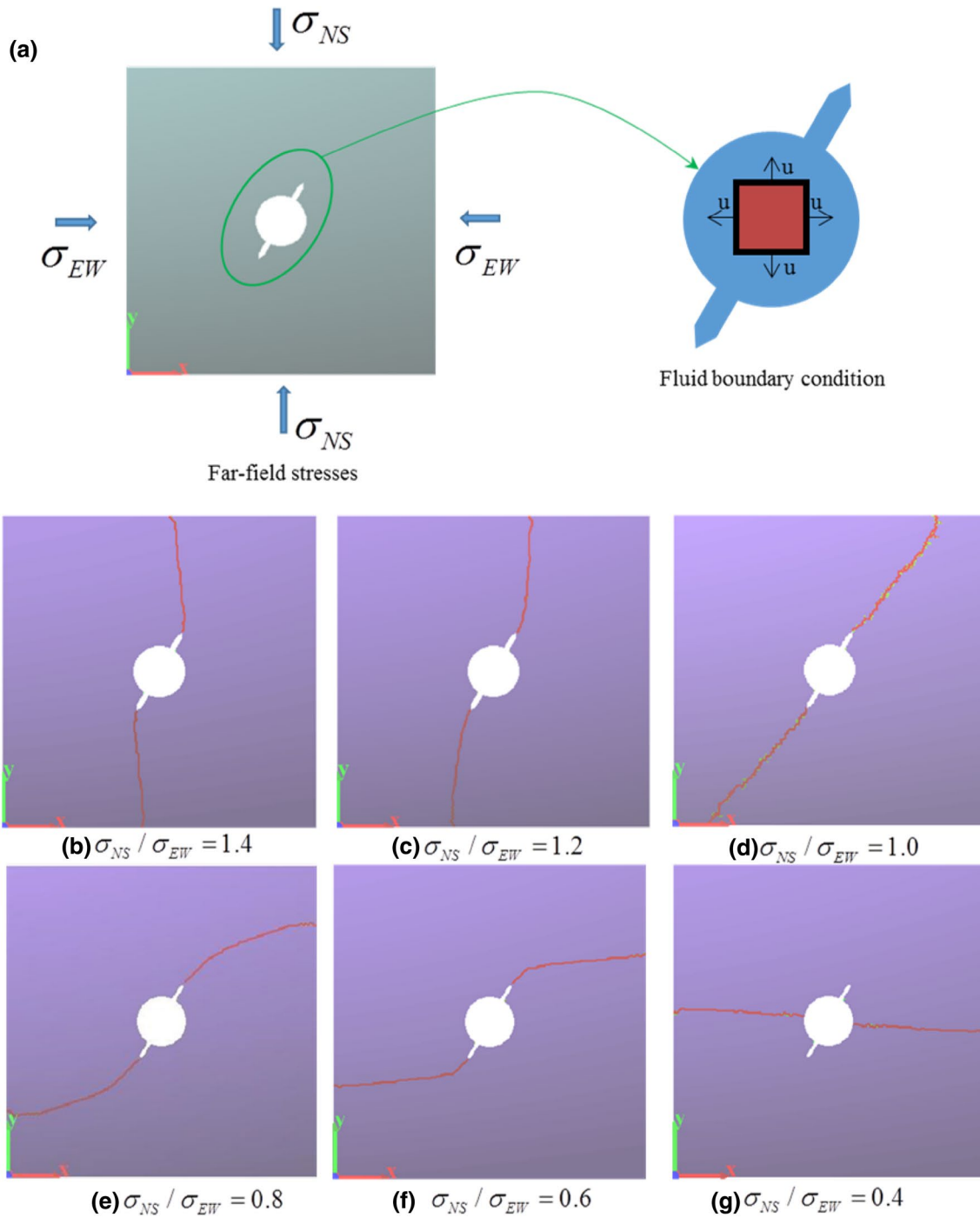


Fig. 14 Non-planar hydraulic fracture propagation with the influence of the deviated far-field stresses. **a** Direction of the far-field stresses and the fluid boundary condition inside the borehole. **b–g** Crack path under different deviated stress ratios

experiment. Since the coupled model is a direct coupling of fluid dynamics with solid dynamics, a full verification of the coupling technique in Sect. 3, together with the observations shown in Fig. 16, leads to the conclusion that the model is able to predict the failure pattern and peak pressures of hydraulic fracturing. This is the main

purpose of numerical simulation of hydraulic fracturing for practical applications, e.g., the analysis of complex hydraulic fracturing in naturally fractured rock masses.

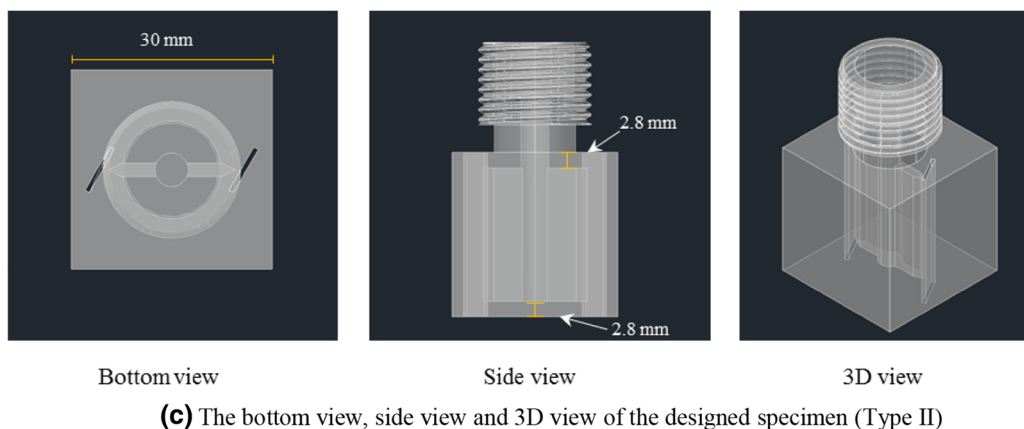
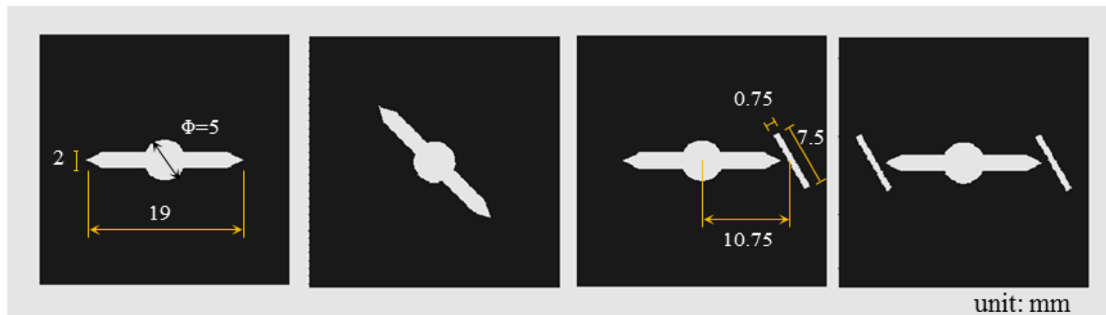
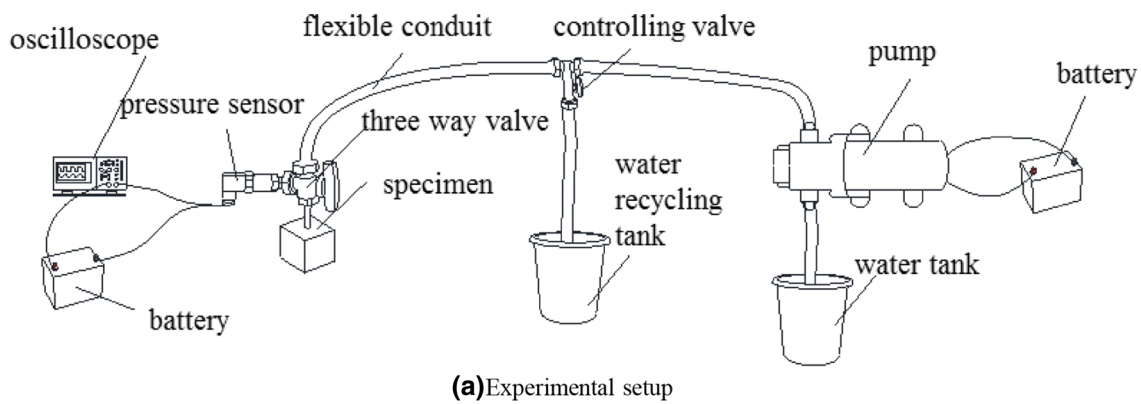
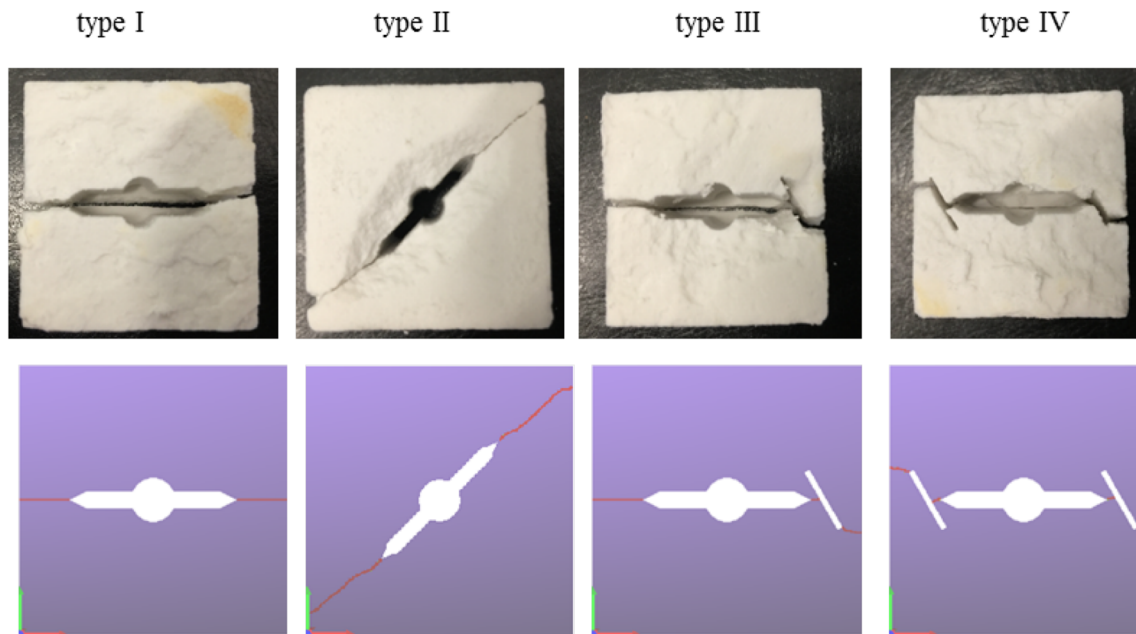


Fig. 15 Hydraulic fracturing tests on 3D printed specimens

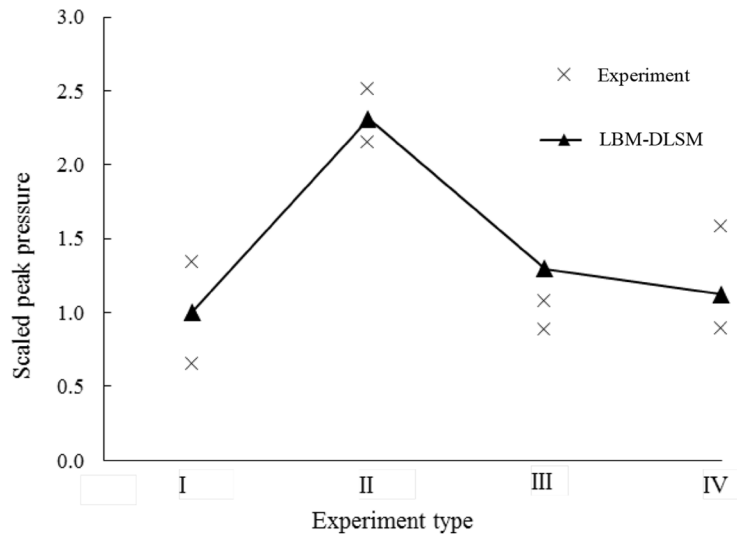
4.3 Hydraulic Fracturing Propagation in a Discrete Fracture Network

In this example, the ability of the model to propagate in a discrete fracture network (DFN) is illustrated. For rock masses, discontinuities are the main controlling factors of their mechanical behaviour (Li et al. 2015; 2017). It is important for a numerical model to consider the inhomogeneity, anisotropy, discontinuity, nonlinearity and progressive failure of the rock. Many efforts have been made to enrich the abilities of the DLSM to represent the mechanical responses of rock, e.g., the mechanical behaviour of 3D rock

joints (Zhao 2015), the nonlinear responses of rock (Jiang and Zhao 2018; Zhao et al. 2019), and the inhomogeneity of rock (Zhao et al. 2014). In this section, the main purpose is to illustrate the applicability of LBM–DLSM coupling in solving complex geometry problems. We did not implement the complex techniques provided in Zhao (2015) to address the joints but used a simplified version instead. Here, joints are represented as 2D lines, and the spring bonds, which were cut by the lines (joints), are set to zero strength. By doing so, the interaction between these joints would be similar to a normal spring contact with zero strength. For the distribution of these joints, a simple distribution law was



(a) Failure patterns



(b) Peak pressures

Fig. 16 Numerical prediction of the hydraulic fracturing test using LBM–DLSM

used, e.g., an even random distribution function was used for the angles and the length of the random joints. Figure 17 describes situations in which three wellbores connected by the pipeline are subject to injection simultaneously. The domain is 300×300 lattice units, the diameter of the wellbore is 20, and the vertical perforation length is three. To ensure that cracks initiate from the perforation tips, natural fractures (NF) are avoided at a certain distance near the pipe. The crack pattern without the influence of the NF is shown in Fig. 17a for reference. In Fig. 17b, fractures with a uniform length of seven are placed in positions, where the

centre-to-centre distance is 10. The cracks in different rows are staggered at $\pm 60^\circ$. This type of DFN guides the fractures in the north–south direction along the regular staggered fractures. In addition, the fast crack propagation from the wellbores at the sides impedes the pressure accumulation near the central wellbore; thus, the fracture length is arrested and is much shorter than the neighbouring fractures. In Fig. 17c, all the NF incline at 60° and are at a length of 12, and the crack propagations tilt once they coalesce to the NF in the neighbouring column. In the cases of Fig. 15d, e, the NF is in random positions with 60° or 45° inclinations, and the

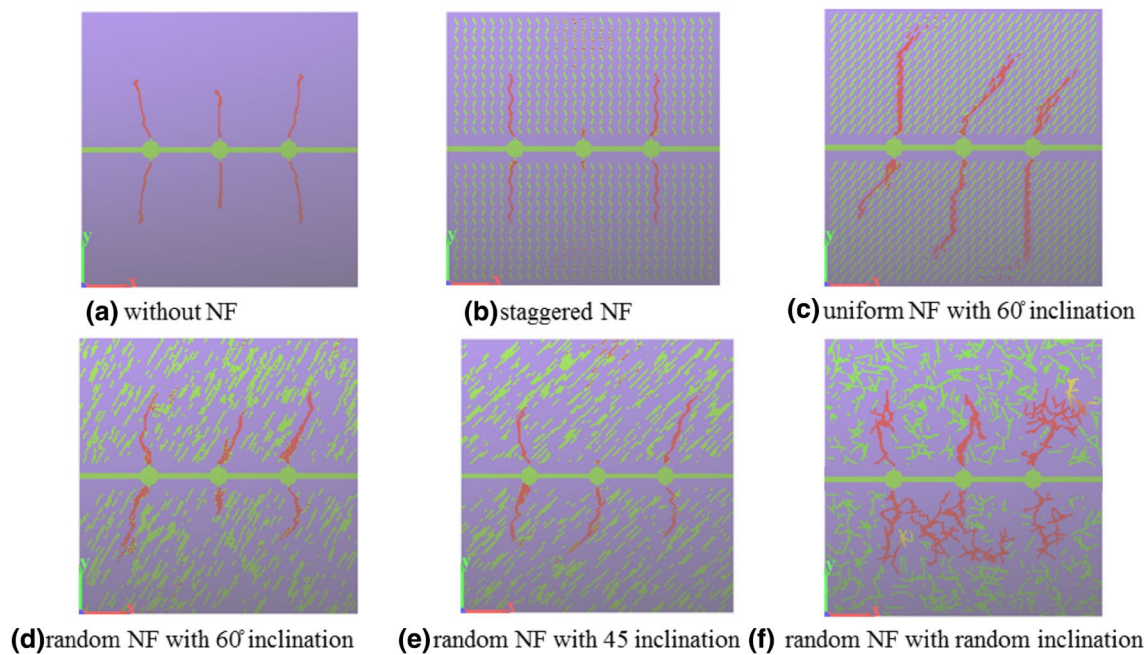


Fig. 17 Hydraulic fracture propagation with the presence of DFN

lengths are randomly chosen from 0 to 20. It is seen that the cracks tend to propagate along the inclination angle once they coalesce with NF. Finally, in Fig. 17f, all the natural fractures are randomly inclined and positioned. A hydraulic fracture network is formed, which is a complex pattern with multiple branches. This type of fracture pattern is favourable in hydraulic fracturing projects for fuel or gas retraction. These examples show that the coupled model can easily cope with DFN.

The coupled model presented in this paper tries to make the best use of the advantages of the DLSSM in fracturing problems and LSM in modelling fluid dynamics. For hydraulic fracturing problems, there are fewer assumptions, e.g., the fluid flow within fractures was a result of fluid dynamic modelling rather than a prescribed Darcy's law. Therefore, it can automatically capture the topological change in the fracture network during fracturing. The practical application of this model would be to study the mechanism of hydraulic fracturing and to provide guidance for the design of hydraulic fracturing equations based on scaled models, e.g., in models using Darcy's law for fluid flow within fractures. Moreover, the coupled model can also be directly used to simulate the fracturing patterns of hydraulic fracturing of joined rock masses under different initial stresses, which are useful in reservoir engineering, where hydraulic fracturing is needed. However, the LBM adopted here is the simplest single-component single-phase BGK model. More realistic scenarios, such as fracturing in dry and porous formations, require multi-phase or even more advanced LBM models. In addition,

this DLSSM is restricted to small deformations; thus, the large fracture openings are not captured. These features can be incorporated into the coupled model in future studies.

5 Conclusion

A new hydro-mechanical model was developed for hydraulic fracturing of rock by direct coupling of the DLSSM and LBM. The main contribution of the model is the coupling scheme of using the fluid–solid interaction by stair-wise momentum exchange bounce-back, which was well verified against other numerical or analytical solutions. The lattice meshes in these two methods overlap, which makes it easy for implementation. The calculation steps are synchronised, which ensures the prompt update of the fluid–solid interaction. The comparisons with a series of benchmark solutions show satisfactory accuracy of the coupled model. The coupled model also successfully simulates an experiment on 3D-printed specimens, as well as crack propagation and coalescences with complex geological conditions. However, our current hydro-mechanical model is only applicable to fully saturated medium. In addition, no vacuum or leak is allowed in the fractures. In the future, these features will be included in the model. In addition, the current solid model is only applicable to small deformations; thus, large deformations need to be

considered. Furthermore, a 3D-coupled model needs to be developed.

Acknowledgements This research is financially supported by the National Natural Science Foundation of China (Grant No. 1177020290).

References

- Adachi J, Siebrits E, Peirce A, Desroches J (2007) Computer simulation of hydraulic fractures. *Int J Rock Mech Min Sci* 44(5):739–757
- Braza M, Chassaing P, Ha MH (1986) Numerical study and physical analysis of the pressure and velocity fields in the near wake of a circular cylinder. *J Fluid Mech* 165(165):79–130
- Buxton GA, Verberg R, Jasnow D, Balazs AC (2005) Newtonian fluid meets an elastic solid: coupling lattice boltzmann and lattice-spring models. *Phys Rev E*. 71(5 Pt 2):056707
- Chen S, Doolen GD (1998) Lattice boltzmann method for fluid flows. *Annual Rev Fluid Mech* 30(1):329–364
- Faxén H (1946) Forces exerted on a rigid cylinder in a viscous fluid between two parallel fixed planes. In: *Proceedings of the Royal Swedish Academy of Engineering Sciences*, vol 187, p 1
- García M, Gutierrez J, Rueda N (2011) Fluid–structure coupling using lattice-Boltzmann and fixed-grid FEM. *Finite Elem Anal Design* 47(8):906–912
- García-Salaberri PA, Gostick JT, Hwang G, Weber AZ, Vera M (2015) Effective diffusivity in partially-saturated carbon-fiber gas diffusion layers: effect of local saturation and application to macroscopic continuum models. *J Power Sour* 296:440–453
- Ghia U, Chia KN, Shin CT (1982) High-Re solutions for incompressible flow using the Navier-Stokes equations and a multigrid method. *J Comput Phys* 48(3):387–411
- Gingold RA, Monaghan JJ (1977) Smoothed particle hydrodynamics: theory and application to non-spherical stars. *Month Not R Astron Soc* 181(3):375–389
- Gui Y, Zhao GF (2015) Modelling of laboratory soil desiccation cracking using DLSM with a two-phase bond model. *Comput Geotech* 69:578–587
- Han Y, Cundall PA (2011) Resolution sensitivity of momentum exchange and immersed boundary methods for solid–fluid interaction in the lattice Boltzmann method. *Int J Numer Meth Fluids* 67(3):314–327
- Han Y, Cundall PA (2013) LBM–DEM modeling of fluid–solid interaction in porous media. *Int J Numer Analyt Meth Geomech* 37(10):1391–1407
- Holmes DW, Williams JR, Tilke P (2011) Smooth particle hydrodynamics simulations of low Reynolds number flows through porous media. *Int J Numer Analyt Meth Geomech* 35(4):419–437
- Hoogerbrugge P, Koelman J (1992) Simulating microscopic hydrodynamic phenomena with dissipative particle dynamics. *EPL* 19(3):155
- Hu HH, Joseph DD, Crochet MJ (1992) Direct simulation of fluid particle motions. *Theor Comput Fluid Dyn* 3(5):285–306
- Inamuro T (2012) Lattice Boltzmann methods for moving boundary flows. *Fluid Dyn Res* 44(2):024001
- Ji C, Munjiza A, Williams JJR (2012) A novel iterative direct-forcing immersed boundary method and its finite volume applications. *J Comput Phys* 231(4):1797–1821
- Jiang C, Zhao G-F (2018) Implementation of a coupled plastic damage distinct lattice spring model for dynamic crack propagation in geomaterials. *Int J Numer Analyt Meth Geomech* 42(4):674–693
- Jiang C, Zhao G-F, Zhu J, Zhao Y-X, Shen L (2016) Investigation of dynamic crack coalescence using a gypsum-like 3D printing material rock mech. *Rock Eng* 49(10):3983–3998
- Jiang C, Zhao G-F, Khalili N (2017) On crack propagation in brittle material using the distinct lattice spring model. *Int J Solid Struct* 118–119:1339–1351
- Kazerani T, Zhao G-F, Zhao J (2010) Dynamic fracturing simulation of brittle material using the distinct lattice spring method with a full rate-dependent cohesive law. *Rock Mech Rock Eng* 43(6):717–726
- Kollmannsberger S, Geller S, Düster A, Tölke J, Sorger C, Krafczyk M, Rank E (2009) Fixed-grid fluid–structure interaction in two dimensions based on a partitioned lattice boltzmann and p-fem approach. *Int J Numer Meth Eng* 79(7):817–845
- Krause MJ, Heuveline V (2013) Parallel fluid flow control and optimisation with lattice Boltzmann methods and automatic differentiation. *Comput Fluids* 80(1):28–36
- Kwon YW (2008) Coupling of lattice Boltzmann and finite element methods for fluid-structure interaction application. *J Press Vessel Tech* 130:011302
- Kwon YW, Jo JC (2008) 3D modeling of fluid-structure interaction with external flow using coupled LBM and FEM. *J Press Vessel Tech* 130(2):021301
- Leonardi A, Wittel FK, Mendoza M, Herrmann HJ (2014) Coupled DEM–LBM method for the free-surface simulation of heterogeneous suspensions. *Comput Particle Mech* 1(1):3–13
- Li JC, Li HB, Zhao J (2015) An improved equivalent viscoelastic medium method for wave propagation across layered rock masses. *Int J Rock Mech Min Sci* 73(1):62–69
- Li JC, Li NN, Li HB, Zhao J (2017) An SHPB test study on wave propagation across rock masses with different contact area ratios of joint. *Int J Impact Eng* 105:109–116
- Lisjak A, Grasselli G, Vietor T (2014) Continuum-discontinuum analysis of failure mechanisms around unsupported circular excavations in anisotropic clay shales. *Int J Rock Mech Min Sci* 65:96–115
- Liu M, Meakin P, Huang H (2007) Dissipative particle dynamics simulation of pore-scale multiphase fluid flow. *Water Resour Res* 43(4):244–247
- Martel C, Iacono-marziano G (2015) Timescales of bubble coalescence, outgassing, and foam collapse in decompressed rhyolitic melts. *Earth Planet Sci Lett* 412:173–185
- Men X, Tang CA, Wang S, Li Y, Yang T, Ma T (2013) Numerical simulation of hydraulic fracturing in heterogeneous rock: the effect of perforation angles and bedding plane on hydraulic fractures evolutions. In: *Bunger AP, McLennan J, Jeffrey R (eds) Effective and sustainable hydraulic fracturing*. InTech, Rijeka
- Mohamad AA, Kuzmin A (2010) A critical evaluation of force term in lattice Boltzmann method, natural convection problem. *Int J Heat Mass Trans* 53(5–6):990–996
- Mora P, Wang Y, Alonso-marroquin F (2015) Lattice solid/Boltzmann microscopic model to simulate solid/fluid systems—a tool to study creation of fluid flow networks for viable deep geothermal energy. *J Earth Sci* 26(1):11–19
- Munjiza A, Owen DRJ, Bicanic N (1995) A combined finite-discrete element method in transient dynamics of fracturing solids. *Eng Comput* 12(2):145–174
- Palabos 1.5R (2017) [http://www.palabos.org/\[Online\]](http://www.palabos.org/[Online]). Accessed April 25 2017
- Richou AB, Ambari A, Naciri JK (2004) Drag force on a circular cylinder midway between two parallel plates at very low Reynolds numbers—part 1: poiseuille flow (numerical). *Chem Eng Sci* 59(15):3215–3222
- Wang H (2015) Numerical modeling of non-planar hydraulic fracture propagation in brittle and ductile rocks using XFEM with cohesive zone method. *J Petrol Sci Eng* 135:127–140

- Wang M, Fen YT, Wang CY (2016) Coupled bonded particle and lattice Boltzmann method for modelling fluid–solid interaction. *Int J Numer Analyt Meth Geomech* 40(10):1383–1401
- Xue S, Yuan L, Wang J, Wang Y, Xie J (2015) A coupled DEM and LBM model for simulation of outbursts of coal and gas. *Int J Coal Sci Tech* 2(1):22–29
- Yin P, Zhao G-F (2015) Numerical study of two-phase fluid distributions in fractured porous media. *Int J Numer Analyt Meth Geomech* 39(11):1188–1211
- Yu D, Mei R, Luo LS, Shyy W (2003) Viscous flow computations with the method of lattice Boltzmann equation. *Prog Aerospace Sci* 39(5):329–367
- Zhang H, Tan Y, Shu S, Niu X, Trias FX, Yan GD, Li H, Sheng Y (2014) Numerical investigation on the role of discrete element method in combined LBM–IBM–DEM modeling. *Comput Fluids* 94(2):37–48
- Zhao G-F (2015) Modelling 3d jointed rock masses using a lattice spring model. *Int J Rock Mech Min Sci* 78:79–90
- Zhao G-F (2017) Developing a four-dimensional lattice spring model for mechanical responses of solids. *Comput Meth Appl Mech Eng* 315:881–895
- Zhao G-F, Khalili N (2012) A lattice spring model for coupled fluid flow and deformation problems in geomechanics. *Rock Mech Rock Eng* 45(5):781–799
- Zhao G-F, Fang J, Zhao J (2011) A 3D distinct lattice spring model for elasticity and dynamic failure. *Int J Numer Analyt Meth Geomech* 35:859–885
- Zhao G-F, Russell A, Zhao X, Khalili N (2014) Strain rate dependency of uniaxial tensile strength in Gosford sandstone by the distinct lattice spring model with x-ray micro CT. *Int J Solids Struct* 51(7–8):1587–1600
- Zhao G-F, Kazerani T, Man K, Gao M, Zhao J (2015) Numerical study of the semi-circular bend dynamic fracture toughness test using discrete element models. *Sci China Tech Sci* 58(9):1587–1595
- Zhao G-F, Lian J, Russell A, Khalili N (2019) Implementation of a modified Drucker-Prager model in the lattice spring model for plasticity and fracture. *Comput Geotech* 107:97–109

Publisher's Note Springer Nature remains neutral with regard to jurisdictional claims in published maps and institutional affiliations.